Astron. Astrophys. 359, 707–715 (2000)

ASTRONOMY AND ASTROPHYSICS

Multiple shells in IRC+10216: shell properties*

N. Mauron[1] **and P.J. Huggins**[2]

[1] Groupe d'Astrophysique, CNRS and Université de Montpellier, Case 072, Place Bataillon, 34095 Montpellier Cedex 05, France
[2] Physics Department, New York University, 4 Washington Place, New York, NY 10003, USA

Received 22 March 2000 / Accepted 26 April 2000

Abstract. We report on the properties of the multiple shells in the circumstellar envelope of IRC+10216, using deep optical imaging, including data from the Hubble Space Telescope. The intensity profiles confirm the presence of thin ($\sim 0\farcs5$–$3''$), limb-brightened shells in the envelope, seen in stellar and ambient Galactic light scattered by dust. The shells are spaced at irregular intervals of $\sim 5''$–$20''$, corresponding to time scales of 200–800 yr, although intervals as short as $\sim 1''$ (40 yr) are seen close to the star. The location of the main shells shows a good correlation with high-resolution, molecular line maps of the inner envelope, indicating that the dust and gas are well coupled. The shell/intershell density contrast is typically ~ 3, and we find that the shells form the dominant mass component of the circumstellar envelope. The shells exhibit important evolutionary effects: the thickness increases with increasing radius, with an effective dispersion velocity of 0.7 km s^{-1} and there is evidence for shell interactions. Despite the presence of bipolar structure close to the star, the global shell pattern favors a roughly isotropic, episodic mass loss mechanism, with a range of time scales.

Key words: stars: AGB and post-AGB – stars: mass-loss – stars: individual: IRC +10216 – stars: circumstellar matter

1. Introduction

Mass loss plays a major role in the evolution of stars on the Asymptotic Giant Branch (AGB). The mass loss history of the stars is recorded, in part, in the structure of their extended circumstellar envelopes, and there is evidence in some cases for deviations from spherical symmetry and important temporal variations. These asymmetries and variations provide crucial information on the mass loss mechanism, and are essential for the correct interpretation of observations of the physical and chemical properties of the envelopes (see, e.g., recent reviews by Olofsson 1999, Lopez 1999, Glassgold 1999).

IRC+10216 is the nearest carbon star with a high mass loss rate. It has been intensively observed at infrared and millimeter wavelengths, and serves as an important archetype for the study of mass loss on the AGB. For the distance we adopt 120 pc (Loup et al. 1993) which is consistent with most recent estimates. The mass loss rate is $\sim 2 \times 10^{-5}$ M$_{\odot}$ yr^{-1}, the terminal expansion velocity of the gas is 14 km s^{-1}, and the molecular envelope can be detected out to $\sim 200''$ from the star (see, e.g., Huggins 1995).

Although IRC+10216 is faint at optical wavelengths, we recently reported deep imaging in B and V with the Canada-France-Hawaii Telescope (CFHT) that provides an extended view of the envelope at arc second resolution (Mauron & Huggins 1999, hereafter Paper I). At these short wavelengths, the envelope is seen in dust-scattered, ambient, Galactic light. The CFHT images show that the envelope consists of a series of nested, multiple shells. The shells are of particular interest because similar structures have been seen in several post-AGB objects (e.g., Terzian & Hajian 2000) where they are remnants from the AGB, illuminated by the central star. The presence of shells in the archetype IRC+10216 provides strong evidence that multiple shells are a common feature of mass loss on the AGB.

IRC+10216 is well suited for a detailed study of the shells because they are relatively evenly illuminated by external radiation and because IRC+10216 is much nearer than any of the more evolved cases, typically by factors of 5–10. In this paper, we examine some aspects of the shells, based on the observations reported in Paper I and archival HST WFPC2 observations which provide a gain in angular resolution of a factor ∼10. The data provide basic constraints on the properties of the shells and their evolution.

2. Observational data

The CFHT observations are described in detail in Paper I. They consist of B and V band images over a large field in which individual shells are identified out to distances of $r \sim 80''$ from the star and the azimuthally averaged envelope is detected out to $r \sim 200''$. The pixel size is $0\farcs44$ and the S/N ratio of the envelope signal (a few percent of the sky background) is ~ 6

Send offprint requests to: N. Mauron

* Based on observations made with the Canada-France-Hawaii telescope, operated by CNRS, NRCC and UH, and on dearchived observations made with the NASA/ESA *Hubble Space Telescope*, operated by AURA Inc., under NASA contract NAS5-26555

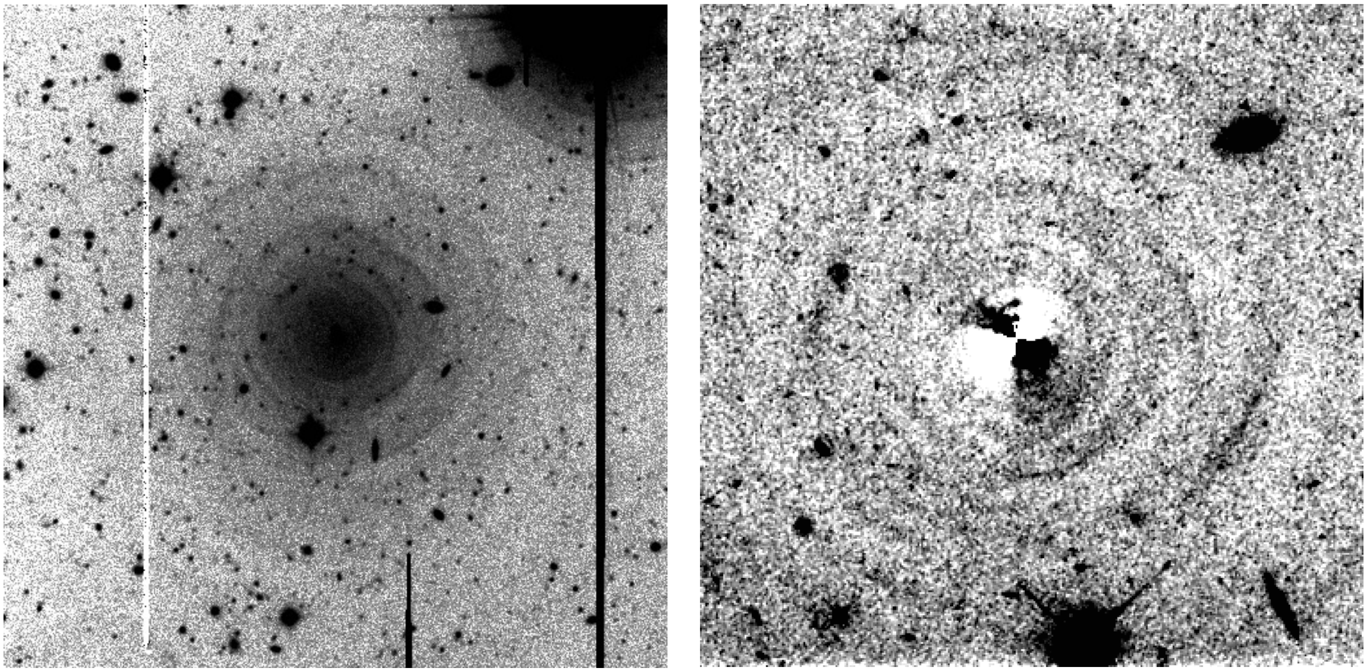

Fig. 1. The multiple shells in IRC+10216. *Left panel:* CFHT V-band image. Field is $223'' \times 223''$, with North to the top, East to the left. *Right panel:* HST WFPC2 wide-V image, with a smooth, radial profile subtracted to enhance visibility of the shells. The field is $74''\!.5 \times 74''\!.5$, rotated 26° counter-clockwise with respect to left panel.

per pixel at $r = 20''$, on the V frame. For reference, the CFHT V band image is shown in the left hand panel of Fig. 1.

The HST observations useful for a study of the shells consist of a series of exposures in the wide-V (F606W) filter. Details are given in the appendix. The final image has a usable field of $74''\!.5 \times 74''\!.5$ of $0''\!.1$ pixels, centered on the star, and the S/N of the envelope is $\sim$ 3 per pixel at $20''$ from the center. An enhanced version of the image with a smooth, azimuthally averaged profile subtracted to emphasize the shell structure, is shown in the right hand panel of Fig. 1.

3. The multiple shell envelope

3.1. Comparison of the CFHT and HST data

The images shown in Fig. 1 provide an overview of the multiple shells in the envelope of IRC+10216. The HST field covers the central regions of the CFHT field and is rotated 26° counter-clockwise. The bright star to the South and the galaxy to the West of the center facilitate the registration. Inspection of the images shows that they exhibit essentially the same basic shell structure (e.g., the prominent arc between the bright star to the South and the galaxy to the West), confirming the presence of the multiple shells reported in Paper I. The resolution is higher but the S/N is lower in the HST image, and the appearance is affected by the slightly longer wavelength of the wide-V filter, which increases the contribution of light from the central star.

The dramatic bi-conical appearance of the center of the HST image occurs because the inner region is dominated by radiation which filters out from the central star along a bipolar axis, and a bipolar shadow is seen out to about $r \sim 15''$. Farther out, the radiation field is dominated by ambient Galactic light, and this is supported by the appearance of bright shells that cross the latitudes of the shadow. In this outer region, the illumination is not strongly directional, and the envelope is seen to be roughly circularly symmetric.

In order to show the shells with maximum clarity, we have also produced a composite image in which we have rotated and rebinned the HST image and combined it with the CFHT image. The result is shown in Fig. 2 with a smooth, radial profile subtracted to enhance the contrast.

As can be seen from Figs. 1 and 2, the main arcs are separated by typically $5''$–$20''$ (which corresponds to time scales of 200–800 yr), and they are prominent over a range $\lesssim 45^\circ$ in azimuth although they may also extend over much larger angles at lower levels. We also note that the individual arcs are often not exactly centered on the star. The fractional radial variation of the arcs, $(r_{\rm max} - r_{\rm min})/r_{\rm mean}$, is distributed between $\sim$ 0 and 12%, with a weak tendency for more circular arcs at larger radii. The non-circularity almost certainly indicates differential bulk motions in the shells up to $\Delta V/V \sim 12\%$, where V is the expansion velocity, or $\Delta V \sim 2$ km s^{-1}.

3.2. The central regions

The prominent bi-conical illumination seen at the center of Figs. 1 (right) and 2 has opening angles of 73° to the North and 81° to the South. The bipolar axis lies at $\mathrm{P.A.} = 8^\circ$ (with respect to true North), in rough agreement with the orientation of structure seen on much smaller angular scales at longer wavelengths (e.g., Haniff & Buscher 1998, Weigelt et al. 1998).

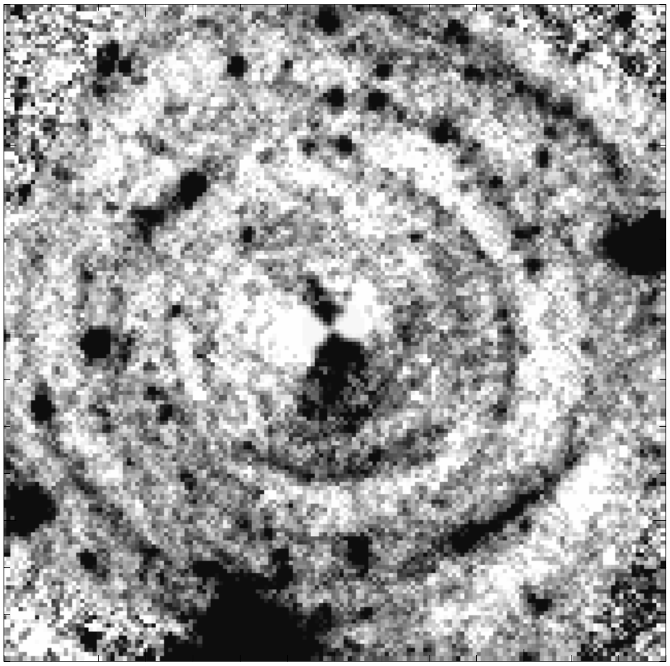

Fig. 2. Composite image of the inner envelope of IRC+10216, made by combining the CFHT V and the HST wide-V band images. The pixel size is $0\farcs44$, and the field is $70'' \times 70''$. North is at the top, East is to the left.

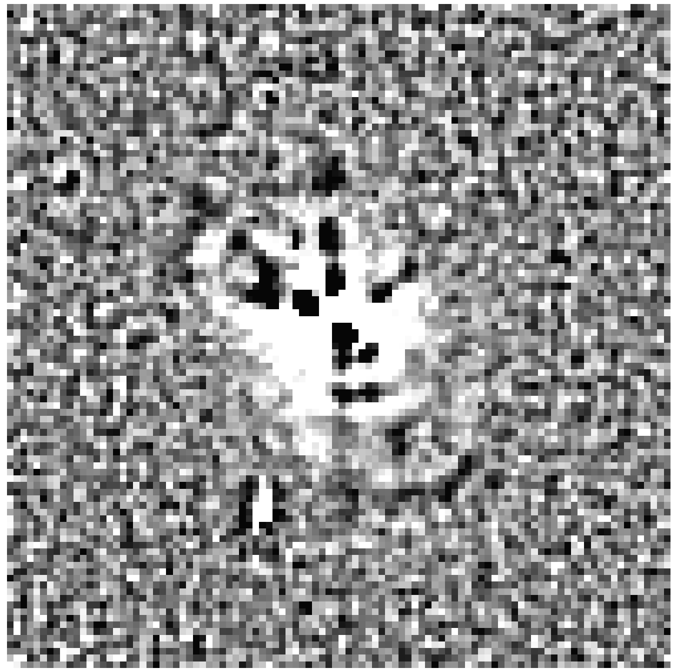

Fig. 3. Central $10'' \times 10''$ field of the HST wide-V band image. North lies 26°counter clockwise from the top. An unsharp mask has been applied to enhance small scale structure (see text).

The direct HST image of these central regions closely resembles the HST image at $\lambda \sim 8140$ Å reported by Skinner et al. (1998). The south lobe ($\sim$ 3700 counts) is brighter than the north lobe ($\sim$ 400 counts) consistent with a tilt in the axis towards us in the South, estimated to be $\sim 20°$ with respect to the plane of the sky by Skinner et al. (1998). In order to emphasize the structure of the central region against the very steep background, we have divided the image by a smoothed version, averaged over 5×5 pixels (Fig. 3). To the south in this image one can see three distinct shells at $r \sim 1\farcs3$, $1\farcs9$, and $3\farcs1$. To the North at similar distances there are several spots, which we interpret as shells, illuminated by narrow beams of radiation from the center, as in CRL 2688 (Sahai et al. 1998). The radial separation of these inner shells and spots is $0\farcs6$–$1\farcs2$, which corresponds to times scales of 25–50 yr.

4. Shell thickness, contrast, and pattern

The detailed properties of the shells provide basic constraints on the origin and evolution of structure in the circumstellar envelope, and here we focus on what can be learned from the present data.

4.1. Shell profiles

First we describe measurement of the radial extent or thickness of the shells which can be determined from the shell intensity profiles in the CFHT and HST images. We emphasize the more prominent arcs in order to ensure adequate S/N. As already noted above, some shells are distinctly non circular, and it is necessary to take this into account to avoid blurring of the profiles that occurs in taking purely radial sectors. Accordingly, we determined the center of curvature for each shell, and measured the azimuthally averaged intensity along curved arcs parallel to the shell, in sectors of 20°–50° wide. Pixels affected by stars, galaxies or other small defects were ignored. Radial bins of $0\farcs5$ ($\sim$1 pixel) were adopted for the CFHT data and $0\farcs2$ (2 pixels) for the HST data, as a compromise between obtaining the highest angular resolution and an adequate S/N ratio. The number of pixels over which these averages are taken is 40–95 (CFHT) and 120–350 (HST), which greatly improves the S/N. Examples of these local profiles, extending $\sim 5''$ inside and outside the peaks, are given in Fig. 4.

The general character of the profiles in Fig. 4 confirms that the arcs are limb-brightened, thin shells, as opposed to linear filaments. To place the scale of the figure in perspective, the peak intensity of scattered light seen towards the center of the envelope (the plateau in Fig. 1, left) is 132 counts in the CFHT image, so the peak intensity of the bottom CHFT profile in Fig. 4 is $\sim 20\%$ of the plateau. Similarly for the HST data, the plateau level is ~ 2.6 counts, so the peak intensity of the bottom HST profile is $\sim$ 20% of the plateau. Note that although the non circularity of the arcs is taken into account in extracting the profiles, the geometrical distortion is not very marked, and for the purpose of analyzing the shells further, we assume them to be circularly symmetric.

Two approaches were used to measure the shell thickness. The first, independent of any assumed model, simply consists of fitting a gaussian to the shell profile, after subtracting a polynomial fit to the background signal. This provides a reasonable fit

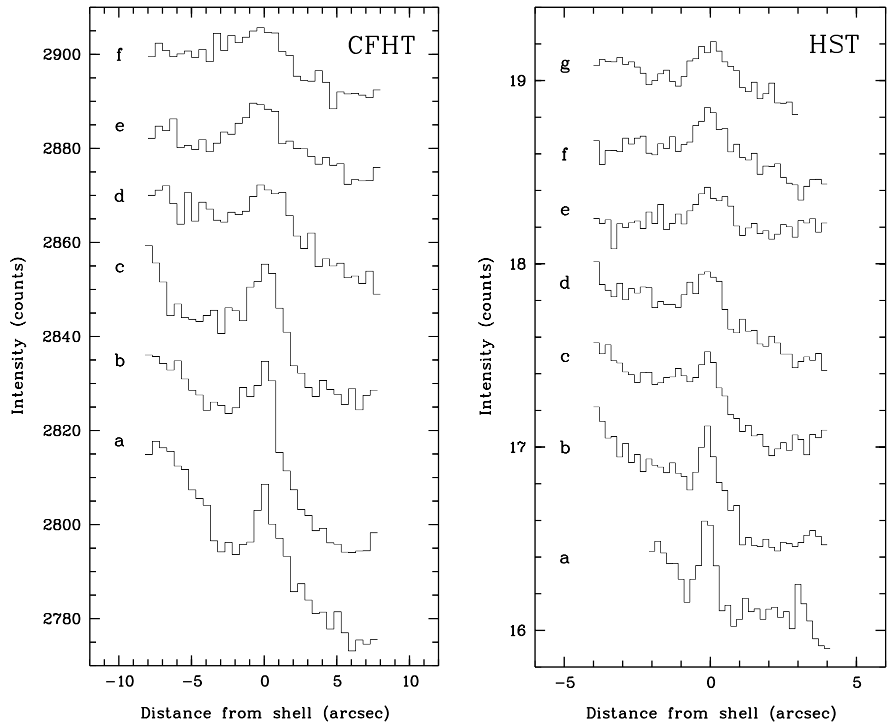

Fig. 4. Intensity profiles of the shells in the CFHT and HST images. The abscissa increases away from the star. For clarity, intensity shifts have been applied to the profiles as follows. CFHT (a–f): −35, 0, +35, +70, +100, +120, and HST (a–g): −1.1, −0.45, +0.35, +0.9, +1.75, +2.2, +2.6. The locations of the shells in radial distance ($''$) from the central star and P.A. from North (min–max in °) are CFHT (a–f): 23$''$ 285°–327°, 27 198–248, 35 297–333, 39 55–101, 55 347–020, 58 23–53; and HST (a–g): 11.5 313–340, 14.3 149–196, 18.7 298–341, 20.0 230–276, 31.5 332–359, 35.0 299–325, 36.0 326–356. Note that CFHT shell c corresponds to HST shell f.

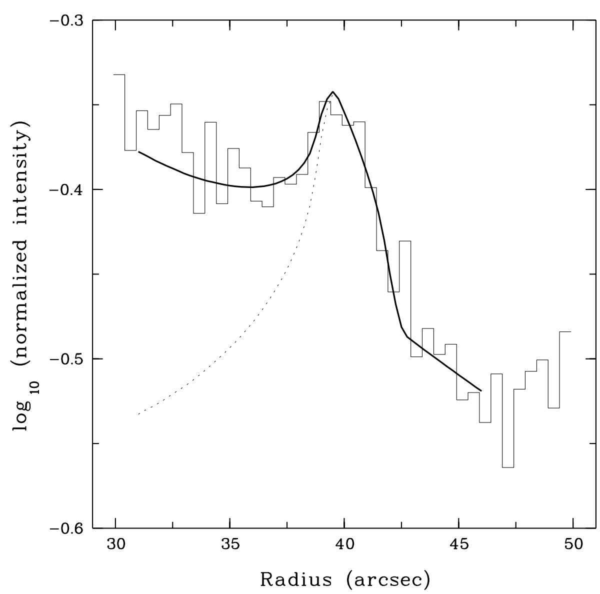

Fig. 5. Shell profile fit. Histogram is the observed CFHT profile labelled d in Fig. 4. Solid curve is model profile with $\Delta r = 3''.0$ and outer/inner contrast of 3.4/2.3. Dotted curve is profile for same model with no material interior to the shell.

in most cases, and gives an apparent thickness $\Delta r_{\rm a}$ (FWHM), which can be corrected by the effect of the point spread function to estimate the shell thickness.

The second approach is to fit a simple shell model to the data, consisting of a background envelope inside and outside the shell, with a constant expansion velocity and constant mass-loss rate (i.e., $n(r) \sim r^{-2}$, where n is the number of dust grains per unit volume), with a narrow shell of enhanced mass-loss forming the shell of thickness Δr. For illumination by the interstellar radiation field in the optically thin limit, the observed intensity is proportional to the column density along any line of sight. Profiles computed from this model, taking into account the effect of the point spread function can then be used to fit the observed profiles. An example of a profile fit is shown by the solid line in Fig. 5. Because the shell thickness determines the rapid rise and fall on the inner and outer edges of the profile, the determination of Δr is rather insensitive to the shell contrast and optical depth (which are discussed further below). For example, the dotted curve in Fig. 5 is for an extreme model where the shell dimensions are the same as for the solid curve, but the interior of the shell is now completely empty: it can be seen that the thickness of the intensity profile is relatively unaffected.

The thickness of the shells estimated by these two methods were consistent, and we were able to measure good shell profiles in 25 cases, several others proving to be too irregular or too noisy. In each case the shell is resolved, with $\Delta r = 0''.5$–$3''$ covering shell radii from 13$''$ to 75$''$ (CFHT) and 10$''$ to 35$''$ (HST). Because of our selection requirements, the results refer to the more prominent shell structures in the envelope. The thickness of the shells is plotted vs. shell radius in Fig. 6, and shows a trend of increasing thickness with radius. This trend is present in the separate CFHT and HST data sets, and can been seen directly in Fig. 4, where the shells are ordered by increasing radius. This effect is discussed further in Sect. 5.

4.2. Shell density contrast

The density contrast between the shells and the intershell regions is a second important characteristic of the envelope that can be obtained from the shell intensity profiles, but is difficult

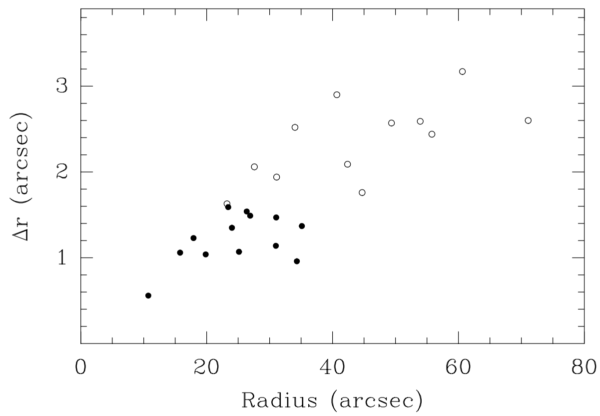

Fig. 6. Variation of shell thickness, Δr, with shell radius. The filled and open circles are HST and CFHT data, respectively.

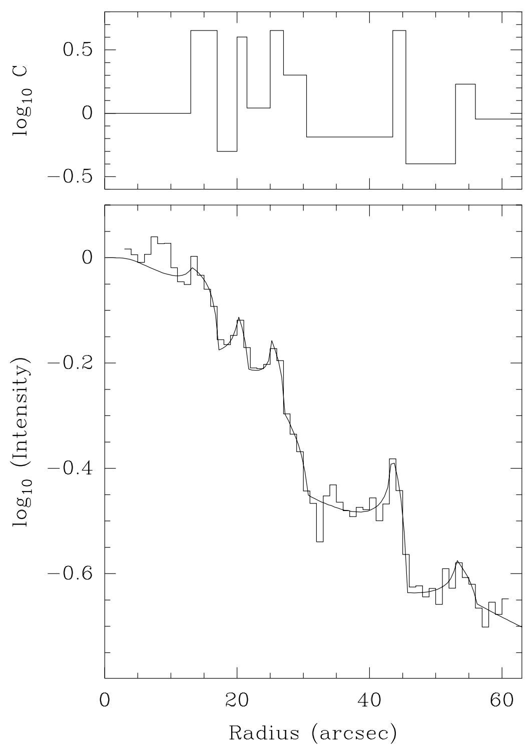

Fig. 7. Multiple shell model fit to radial intensity profile. *Lower panel*: Histogram is observed radial intensity profile at $\mathrm{P.A.} = 214^\circ$ from Paper I; solid line is multiple shell model fit. *Upper panel*: Density contrast in the model fit, expressed as the relative mass-loss rate, C, where $n = Cr^{-2}$. Note that details of the profile have not been fit for $r < 15''$ because of the high optical depth.

to determine in detail because of the large variation among the shells. One simple approach is to assume that each shell is superposed on a smooth envelope background, and this was the model adopted in the previous section, assuming optically thin conditions. The shell-intershell contrast determined for the case shown in Fig. 5 is 2.3 and 3.4 when compared to the envelope interior and exterior to the shell, respectively. For the other cases examined in this way, the contrast is typically 2–3.

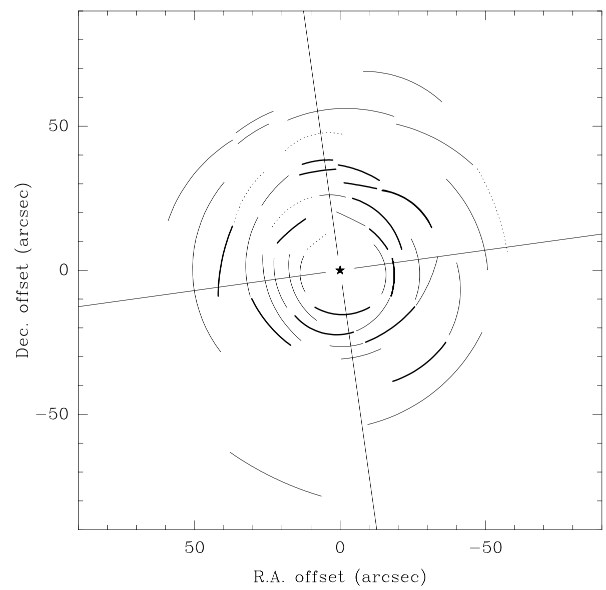

Fig. 8. Overview of multiple shell pattern in the envelope of IRC+10216 from the HST and CFHT observations. Heavier lines denote the more prominent arcs.

A more complete approach, taking into account the overlap of shells along the line of sight, is illustrated in Fig. 7. Here we model an extended radial intensity profile of the envelope, for $\mathrm{P.A.} = 214^\circ$, taken from the CFHT data in Paper I. The shell and intershell regions are all taken to be characterized by $n(r) = Cr^{-2}$, where C is the relative mass loss rate in each region. The shells are assumed to be complete, which overestimates their contribution to the general profile since they tend to be prominent over a limited azimuthal angle, but this is roughly compensated by the fact that other shells will also contribute which are not seen as prominent arcs when they do not intersect the plane of the sky. The optical depth of the shells is taken into account using the analytic solution to the radiative transfer equation for external illumination for any scattering angular distribution function when the albedo $a = 1$. In this case the observed intensity is given by $I = I_{\mathrm{o}}(1 - e^{-\tau})$, where τ is the optical depth along the line of sight and I_{o} is the interstellar field (see Mattila 1970). This expression gives an excellent approximation to the more complete radiative transfer problem for a homogeneous envelope (Martin & Rogers 1987) and to the observed, averaged, radial profile reported in Paper I. For the model calculations, the column density is related to the optical depth along the line of sight by requiring that τ approaches 1 near $R = 10''$ where the average intensity profile reaches a level plateau equal to the ambient radiation field (see Paper I for details).

The shell intensity profile calculated in this way is fit to the observed profile in the lower panel of Fig. 7. The upper panel shows the corresponding density contrast in terms of the scaling parameter C. It can be seen that the shell/intershell contrast varies up to a factor of 10 for the most prominent arc, but is more typically ~ 3, consistent with the simpler estimates discussed above.

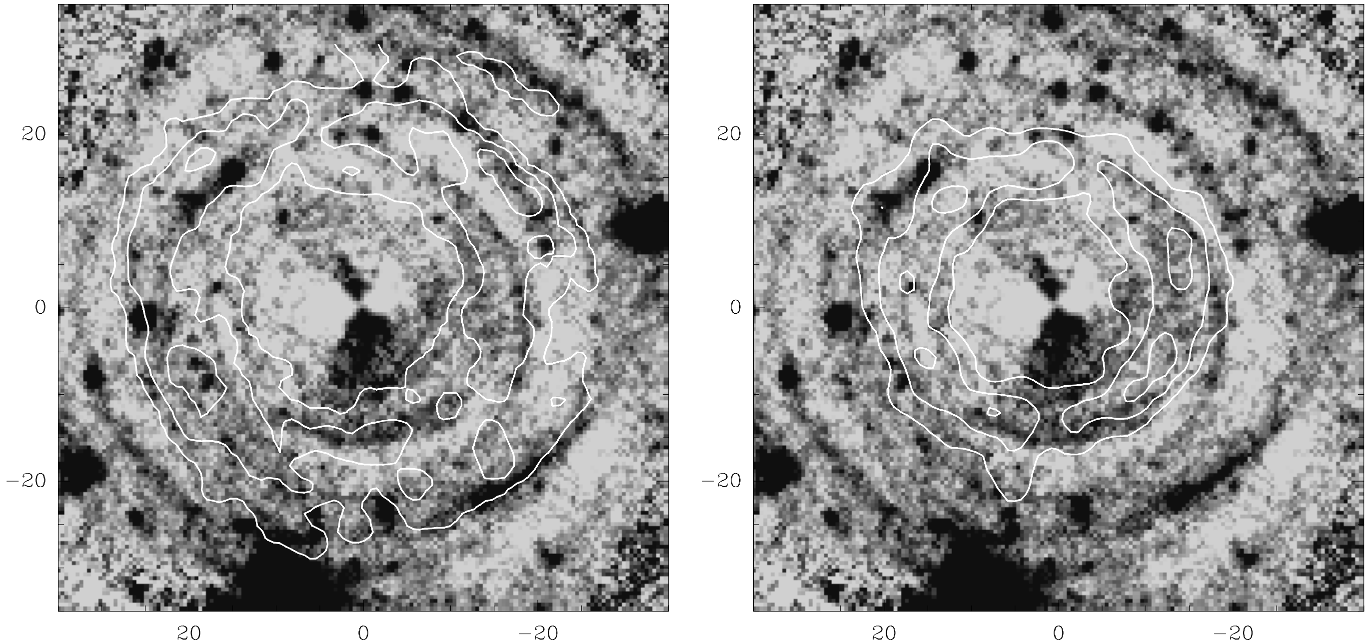

Fig. 9. Comparison of the gas and dust shells in IRC+10216. The white contours represent the distribution of millimeter molecular line emission in CN (*left panel*) and C_3H (*right panel*) from Lucas & Guélin (1999), superposed on a greyscale dust image based on Fig. 2. The axes are labelled with offsets in arcseconds from the center.

4.3. Global pattern

Because the complete shell pattern is not well seen in any single image, we show a sketch of the envelope in Fig. 8 which summarizes the main features. The straight lines passing through the center indicate the bipolar axis measured in Sect. 3.2, and the corresponding equatorial plane perpendicular to this. As can be seen from the figure, there is no obvious symmetry about either axis.

One striking aspect of the overall pattern is the irregular shell spacing. The main arcs are separated by $\sim 5''$–$20''$, corresponding to time scales of 200–800 yr, but there is also smaller scale structure. Only in the SE quadrant out to $r \sim 25''$ are the shells roughly evenly spaced (by $\sim 3''$–$4''$), but elsewhere this is not the case. There is also a tendency for a lack of close spacing at larger radii, and there are distinct examples where non circular shells intersect with other shells (e.g., at $34''$ NW, and $30''$ SW), which point to shell interactions.

5. Relation to the circumstellar gas

In addition to providing a detailed picture of the dust shells, the observations offer a unique opportunity to study the relation of the dust to the gas in the envelope. Under the influence of the radiation field of the star, the dust is expected to drift through the gas with a velocity $v_{\rm d}$. For steady state conditions and a number of simplifying assumptions (e.g., $v_{\rm d} \gg v_{\rm thermal}$), the drift velocity is given by: $v_{\rm d} = (LVQ/\dot{M}c)^{0.5}$, where L is the luminosity, V is the expansion velocity, $\dot{M}$ is the mass loss rate, and Q is the momentum transfer efficiency (Kwan & Linke 1982). For the parameters of IRC+10216, the drift velocity is expected to be ~ 2 km s^{-1} in the case of a homogeneous envelope. In the presence of discrete shells, however, the dust will move ahead of the gas with which it was ejected, and can interact with shells farther out.

The detailed distribution of the gas in the envelope of IRC+10216 is not known, but a rich structure is evident in high resolution millimeter maps of molecular emission, made with the IRAM interferometer (see Guélin et al. 1996, and Lucas & Guélin 1999). The molecular emission is modulated by the excitation of the transition and by circumstellar chemistry, but there are sufficient similarities between the maps of different molecular species that the locations of density enhancements can be inferred.

We examine the relation between the dust and gas in Fig. 9 by comparing the optical image from Fig. 2 with maps in the CN (1–0) and the C_3H (9/2–7/2) lines, which are representative of emission from different classes of molecules. The molecular maps are adapted from Lucas & Guélin (1999). The resolution is $\sim 3''$ and the contours simply represent the overall distribution and the location of peaks of the observed emission near the systemic velocity, which approximately corresponds to the envelope in the plane of the sky. For more detailed information and maps of several other species, see Guélin et al. (1996), and Lucas & Guélin (1999).

Fig. 9 shows that the distribution of dust and gas in IRC+10216 exhibit a remarkable degree of correlation. In CN (left panel), the prominent CN peak to the NW at $r \sim 20''$ is elongated and lies along a dust shell; closer in, a hemispherical ridge of CN at $r \sim 16''$ from N to S also corresponds to connected dust shells. Farther out, arcs of CN to the NW at $r \sim 28''$ and the SW at $r \sim 26''$ lie along, but slightly inside, prominent dust arcs; since this is the edge of the CN distribution, the slight positional displacements probably reflect modulation of the emission by photo-dissociation. To the East, the detailed correspondence is less clear because the dust shells are less distinct and closer together; nevertheless, there is a general correlation between the CN emission and the dust here as well. The C_3H (Fig. 9, right panel) which is characteristic of species which peak at $r \sim 16''$ shows a similar correspondence with the dust, which again is especially clear on the West side where the dust shells are more separate.

The similar peak positions and overall pattern of the dust and molecular emission imply that the dust and gas have not substantially decoupled (in the region covered by the figure) since their ejection from the star. For a dust drift velocity as large as 2 km s^{-1} quoted above, the dust peaks would lie $3''$ outside the gas peaks at $r = 20''$, and this can be reasonably ruled out by inspection of Fig. 9. The explanation is presumably that the drift velocity is lower in the dense shells because of the higher local density, so the dust is more strongly coupled to the gas than it would be in the completely homogeneous case. Higher resolution observations of the gas will allow this interesting issue to be explored in more detail.

6. Shell formation

6.1. Evolution

The observations described above reveal several important characteristics of the shell structure in IRC+10216. We first note that the shells are not cosmetic effects in the envelope. If we take the simple multiple shell model described in Sect. 4, the mass in the shells is $\sim 70\%$ of the total, including the shells and the intershell regions. Although the exact fraction is uncertain because we do not know the detailed structure, we conclude that the shells are the dominant mass component of the envelope.

The properties of the shells provide strong evidence for the evolution of the shells within the circumstellar envelope after they have been ejected by the star. One aspect of the evolution is the dispersion of the shells which is expected on very general hydrodynamic grounds and this is directly observed in the increase of Δr with shell radius in Fig. 6. The increase is roughly linear, albeit with a large scatter, with $\Delta r \sim 0.05\,r$. Since $r \sim Vt$, where t is the age of each shell, this also corresponds $\Delta r \sim \Delta V t$, where ΔV is the effective dispersion velocity whose value is given by $\Delta V \sim 0.05\,V$ or 0.7 km s^{-1}. Physical processes that will contribute to the dispersion include turbulence and differential grain drift velocities (which depend on the grain size and local gas density), as well as the effects of shell merging. It is interesting to note that the velocity dispersion of the gas has been measured from molecular line profiles of the envelope and is found to be $\Delta V(\mathrm{FWHM}) = 0.9$ km s^{-1} (Huggins & Healy 1986), remarkably similar to that estimated here for the dust.

The dispersion of the shells also implies that the shells are quite thin when they are ejected from the star. If we extrapolate the slope in Fig. 6 back to small radii, Δr will be $\lesssim 0\overset{''}{.}5$ which corresponds to a thickness $\lesssim 10^{15}$ cm, or a time scale of $\lesssim 20$ yr. This is consistent with timescales of decades found for episodic dust formation by several AGB stars (Danchi et al. 1994).

A second aspect of shell evolution is the possibility of shell interactions. We have already noted several relevant observations: the tendency of the arcs to be more circular at large radii (Sect. 3.1), the tendency for a lack of small spacing at larger radii, the very narrow shell spacing ($\sim 1''$) seen close to the star ($r \sim 1''$–$3''$) in Fig. 3, and clear examples of shells touching (Fig. 2). When we consider all these, we are lead to the conclusion that shell interactions could, and probably do, make a contribution to the structure seen in the envelope. For example, slightly faster or slower dense shells, might sweep up less dense shells. Judging by the velocity variations implied by non-circular arcs, these effects might sweep regions $\Delta r \sim 0.12r$, and the effects could be greater close to the star. The details of such a picture merit further study.

6.2. Origin

Various models have been proposed for the origin of discrete shells in circumstellar envelopes, and we outlined those which might be relevant to IRC+10216 in Paper I (see also Sahai et al. 1998 in connection with the shells around CRL 2688). We focus here on the constraints offered by the current results.

One popular class of models rests on the effects of a binary companion. In the model by Harpaz et al. (1997) which was devised for CRL 2688, the binary companion in an eccentric orbit modulates the mass loss to produce shells. Predictions of the model include the strict regularity of the shells, and a shell width that increases with time (or decreasing shell radius). The former is not consistent with our observations, and the latter is contrary to what we observe.

A more recent model for the formation of shell structure has been proposed by Mastrodemos & Morris (1999) in which a close binary gives rise to a spiral shock covering most of the solid angle surrounding the star. Three aspects of the observations of IRC+10216 address this model. First, the irregular arc spacing that we observe is not a feature of the model, whose underlying binary mechanism gives rise to a highly regular structure. Second, there is no evidence for a half period mismatch of the shells along the poles of the bipolar axis. There is indeed a distinct gap in the shell structure to the North at $r \sim 20''$, seen in the dust and in some of the molecular maps, but at larger radii and to the south the arcs appear continuous across the bipolar axis. A third expectation from the model is some degree of reflection symmetry about the equatorial plane in cases seen close to edge-on (which is the case for IRC+10216): no such effects are evident in Fig 8. It is possible that the evolutionary effects noted above could mask all these features of the model, but at the moment there is no strong evidence to support it.

A different scenario that indirectly involves a companion, has recently been proposed by Soker (2000), based on mass loss regulated by the presence of magnetically active, cool portions of the rotating photosphere. This gives semi-periodic mass loss but detailed predictions for the shells remain to be worked out before the observations can be considered positive support for this mechanism.

For the case of IRC+10216, we emphasize two things. First, the importance of shell evolution in relating the observed shell patterns to the mass loss mechanism. Second, the presence of a wide range of shell spacing, corresponding to time scales as short as 40 yr (close to the star) and as long as 800 yr. Any consistent model needs to account for this.

7. Conclusions

The observations reported here confirm the presence of a complex, multiple shell structure in the circumstellar envelope of the archetype AGB star IRC+10216. This structure is important because it is likely a common feature of mass loss on the AGB and offers crucial insights into the mass loss mechanism.

In IRC+10216, the shells are spaced at irregular intervals, and show a good correlation with high resolution molecular line maps of the inner envelope, indicating that the dust and gas are well coupled. The shell/intershell density contrast is ~ 3, and we find that the shells form a major mass component of the envelope. The shells show effects of evolution within the envelope, including shell interaction and shell dispersion, with a dispersion velocity of 0.7 km s^{-1}. These observations place basic constraints on the mass loss process and shell formation. They favor a mechanism that is isotropic, with a broad range of time scales.

Acknowledgements. The authors thank the referee, Dr. Winters, for valuable remarks. HST images distributed by the Space Telescope European Coordinating Facility (ESO-ESA) were used. This work was supported in part by the CNRS program *Physico-chimie du Milieu Interstellaire* (N.M.), and by the NSF grant AST96-17941 (P.J.H.).

Appendix A: HST archival data

The HST observations of IRC+10216 were retrieved from the HST data archive, Project No. 6856. They consist of six images obtained with the Wide Field Camera (WFPC2) on 1998/3/30, using the F606W wide-V filter. Each image consists of four panels on the field, but only the panel centered on the star is useful, consisting of 800×800 0.″1 pixels. Five of the images have exposure times of 800 s, and one of 700 s. They have been processed by the latest version of the calibration pipeline, which includes standard corrections such as bias subtraction, flat-fielding, etc. On these individual images, the central core peaks at $\sim$ 4000 counts (cts), but the intensity quickly falls to typically 16–18 cts at distances $r \gtrsim 8''$. The signal from the envelope in these outer regions is only 2–3 cts, and the standard deviation is typically 1.8 cts, so the individual images have a S/N $\sim$ 1–2.

The images are severely affected by cosmic ray events which, when small, can mimic faint stars or galaxies. The strongest hits were removed by using simple comparisons between the images. The images were then merged with a median filter, taking into account the dithered pointing, which eliminates most of the small cosmic rays hits still present. Unusable margins were discarded, and the resulting image consists of 745×745 0.″1 pixels.

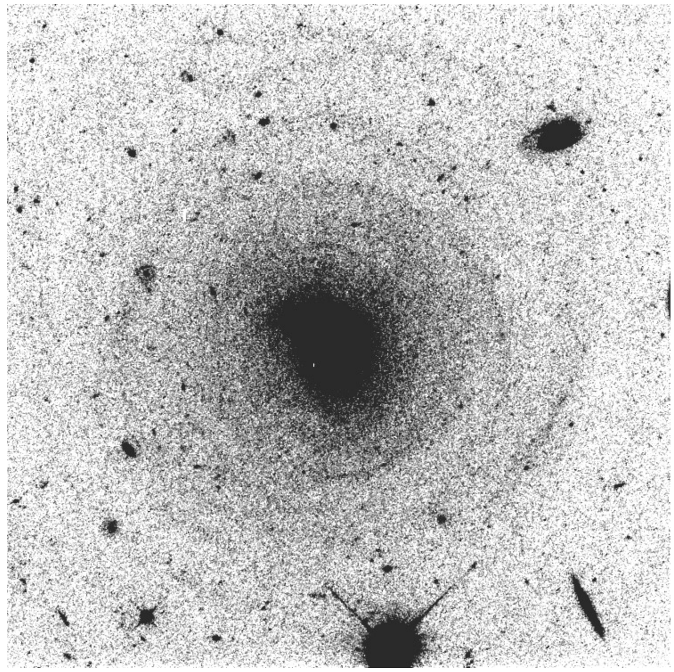

Fig. A.1. HST WFPC2 wide-V image of IRC+10216, with a logarithmic transfer function. The image is $74.''5 \times 74.''5$ with $0.''1$ pixels, oriented with North 26° counter-clockwise from the top.

The final image is shown in Fig. A.1 of the appendix. The display is logarithmic, with lower and upper intensity levels of 16.2 to 18.2 cts, respectively. The standard deviation away from center is 0.50 cts. The star at the bottom of the field is saturated (~ 4000 cts), and the spiral galaxy at the upper right peaks at ~ 90 cts. Comparison with the CFHT images in Paper I, shows that most of the small structures in the image can be identified as stars or galaxies. In order to enhance faint features, an azimuthally averaged and smoothed profile has been subtracted, using as center the brightest point in the core, although this might not be exactly the star location. This image is shown in the right hand panel of Fig. 1 of the paper.

References

Danchi W.C., Bester M., Degiacomi C.G., Greenhill L.J., Townes C.H., 1994, AJ 107, 1469

Glassgold A.E., 1999, Circumstellar Chemistry of AGB Winds. In: Le Bertre T., Lèbre A., Walkens C. (eds.), Proc. IAU Symp. 191, Asymptotic Giant Branch Stars. IAU & Astr. Soc. of the Pacific, p. 337

Guélin M., Lucas R., Neri, R., 1996, Mass Loss in AGB Stars. In: Latter W.B., Radford S.J.E., Jewell P.R., Mangum J.G., Bally J. (eds.) Proc. IAU Symp. 170, CO: Twenty-five Years of Millimeter-Wave Spectroscopy. Kluwer, Dordrecht, p. 359

Haniff C.A., Buscher D.F., 1998, A&A 334, L5

Harpaz A., Rappaport S., Soker N., 1997, ApJ, 487, 809

Huggins P.J., 1995, Ap&SS 224, 281

Huggins P.J., Healy A., 1986, ApJ 304, 418

Kwan J., Linke R.A., 1982, ApJ 254, 587

Lopez B., 1999, AGB and post-AGB Stars at High Angular Resolution. In: Le Bertre T., Lèbre A., Walkens C. (eds.), Proc. IAU Symp. 191, Asymptotic Giant Branch Stars. IAU & Astr. Soc. of the Pacific, p. 409

Loup C., Forveille T., Omont A., Paul J. F., 1993, A&AS 99, 291

Lucas R., Guélin M., 1999, Millimeter-wave Interferometry of Circumstellar Envelopes. In: Le Bertre T., Lèbre A., Walkens C. (eds.) Proc. IAU Symp. 191, Asymptotic Giant Branch Stars. IAU & Astr. Soc. of the Pacific, p. 305

Martin P.G., Rogers C., 1987, ApJ 322, 374

Mastrodemos N., Morris M., 1999, ApJ 523, 357

Mattila K., 1970, A&A 9, 53

Mauron N., Huggins P.J., 1999, A&A 349, 203 (Paper I)

Olofsson H., 1999, The AGB-star Phenomenon: Setting the Stage. In: Le Bertre T., Lèbre A., Walkens C. (eds.), Proc. IAU Symp. 191, Asymptotic Giant Branch Stars. IAU & Astr. Soc. of the Pacific, p. 3

Sahai R., Trauger J.T., Watson A.M., et al., 1998, ApJ 493, 301

Skinner C.J., Meixner M., Bobrowsky M., 1998, MNRAS 300, L29

Soker N., 2000, ApJ (in press)

Terzian Y., Hajian A.R., 2000, Planetary Nebulae with the Hubble Space Telescope. In: Kastner J.H., Soker N., Rappaport S. (eds), Asymmetrical Planetary Nebulae II: From Origins to Microstructures. ASP Conf. Ser., vol. 199, p. 33

Weigelt G., Balega Y., Bloecker T., et al., 1998, A&A 333, L51